Journal of
Applied Crystallography

ISSN 0021-8898

Received 31 October 2006
Accepted 14 March 2007

Scattering from laterally heterogeneous vesicles. II. The form factor

Vinicius N. P. Anghel,[a] Norbert Kučerka,[b,c] Jeremy Pencer[b]* and John Katsaras[b,d,e]

[a]Atomic Energy of Canada Ltd, Chalk River Laboratories, Chalk River, ON, K0J 1J0, Canada, [b]National Research Council, Canadian Neutron Beam Centre, Chalk River Laboratories, Chalk River, ON, K0J 1J0, Canada, [c]Department of Physical Chemistry of Drugs, Faculty of Pharmacy, Comenius University, 832 32 Bratislava, Slovakia, [d]Department of Physics, Biophysics Interdepartmental Group, and Guelph-Waterloo Physics Institute, University of Guelph, Guelph, ON, N1G 2W1, Canada, and [e]Department of Physics, Brock University, 500 Glenridge Avenue, St Catharines, ON, L2S 3A1, Canada. Correspondence e-mail: jeremy.pencer@nrc.gc.ca

Despite growing interest in the formation of domains or 'rafts' in cell and model membranes, there have been relatively few attempts to characterize such systems *via* scattering techniques. Previously [Pencer *et al.* (2006). *J. Appl. Cryst.* **39**, 293–303], it was demonstrated that the Porod invariant, Q, could be used to detect lateral segregation. Here, the general theory for scattering from laterally heterogeneous vesicles is outlined and form factors are derived for vesicles containing either single circular or annular domains. These form factors are then applied to the analysis of neutron scattering data from heterogeneous vesicles. Potential advantages and limitations of this technique are also discussed.

1. Introduction

The term lipid 'rafts' describes putative domains in cell membranes, enriched in cholesterol and saturated sphingolipid, and depleted of unsaturated and polyunsaturated lipids (Edidin, 2001). These rafts have been postulated to play important roles as sites for the transfer of information and material between cells, and also as sites for infection by viruses, such as HIV and Ebola. Model membranes constructed to investigate the lipid-related mechanisms for raft formation typically contain three elements: a long-chain saturated phospho- or sphingolipid, cholesterol (or a structurally related sterol), and an unsaturated, polyunsaturated or short-chain lipid.

The most compelling evidence for the presence of lateral heterogeneities or rafts (*i.e.* phase coexistence) in model membranes comes from fluorescent light microscopy studies of micrometre-sized or giant unilamellar vesicles (GUVs) (see *e.g.* Korlach *et al.*, 1999; Bagatolli & Gratton, 2000; Dietrich *et al.*, 2001). In these studies, GUVs are formed from lipid mixtures which potentially show phase separation and their domains are detected *via* the preferential partitioning of fluorescent probes into one phase over the other. For GUVs composed of two lipid components, heterogeneities are the result of liquid disordered (ld or fluid) and solid ordered (so or gel) phase coexistence, while ternary (lipid–lipid–sterol) mixtures show coexistence between liquid ordered (lo) and ld phases. In the case of solid–liquid coexistence, the higher-melting-temperature lipid is enriched in the solid phase and depleted from the liquid phase. For liquid–liquid coexistence, cholesterol and saturated lipid are enriched in the liquid ordered phase and depleted from the liquid disordered phase.

The general findings from fluorescence microscopy studies are that the formation of domains depends both on membrane composition and temperature (Veatch & Keller, 2003), and that liquid or solid domains can exhibit a variety of morphologies, including circular domains (Veatch *et al.*, 2004), intersecting stripes (Li & Cheng, 2006), regular arrangements of circular or striped domains (Baumgart *et al.*, 2003) and irregular patches (Feigenson & Buboltz, 2001). In general, irregular domains are seen in solid–liquid coexisting systems (*i.e.* in binary mixtures) (Bagatolli & Gratton, 2000), while for liquid–liquid phase coexistence (*i.e.* in ternary or model 'raft' forming mixtures) domains are circular, driven by line tension (Veatch *et al.*, 2004), although Baumgart *et al.* (2003) have also observed striped domains in raft mixtures. Interestingly, it is not clear from these studies whether the variety of domain shapes observed reflects differences in the innate equilibrium behaviour of these systems, or merely differences in their kinetics. In the case of liquid–liquid coexistence, Yanagisawa *et al.* (2007) have shown that vesicles having single circular domains are most likely in their equilibrium state. Recent studies have also demonstrated that even very small amounts (∼0.5 mol%) of fluorescent probe can dramatically change the phase behaviour of mixtures (Veatch *et al.*, 2007), leading to the question of whether these probes also influence domain morphology.

Besides the potential variation of domain morphologies in model systems, further complications arise in characterizing domains due to potential variation in both the length scales and lifetimes of the domains in model *versus* cell membranes (Jacobson *et al.*, 2007). While micrometre-sized domains with lifetimes between minutes and hours are observed in model membranes, it is believed that domains or rafts in cell membranes are transient, having lifetimes as short as microseconds and sizes as small as nanometres (Mayor & Rao, 2004).

As we have discussed (Pencer *et al.*, 2005), a variety of experiments on model and cell membranes have led to two possibly different categories of heterogeneity: (i) large (micrometre-sized) stable domains, readily observable by fluorescence microscopy, and with compositions defined by equilibrium thermodynamics (*i.e.* the tie lines that can be constructed in binary and ternary phase diagrams), and (ii) small (nanoscopic) domains which could either be stable and defined by the same rules as in (i), or transient, with variable composition and lifetimes.

Scattering techniques, such as diffraction and small-angle scattering, using either neutrons or X-rays, show promise in characterizing membrane domains, since the techniques are able to span the length scales intermediate between micrometres and nanometres. Neutron scattering, furthermore (*via* selective deuteration), is sensitive to heterogeneities in membrane composition, and provides direct structural characterization of membrane heterogeneity. As discussed earlier (Pencer *et al.*, 2005), the investigation of membrane domains by small-angle neutron scattering (SANS) thus presents a unique opportunity to determine whether nanoscopic domains in model membranes are equivalent to their microscopic counterparts, or are better classified as short length-scale fluctuations in local composition.

Previously, we demonstrated the efficacy of the SANS method to characterize membrane heterogeneities (Pencer *et al.*, 2005), and more recently, derived a model independent SANS method for the detection of membrane domains (Pencer *et al.*, 2006*a*). While there have been a number of previous attempts to characterize heterogeneous unilamellar vesicles (ULVs) by SANS (Knoll *et al.*, 1981; Czeslik *et al.*, 1997; Nicolini *et al.*, 2004; Pencer *et al.*, 2005; Hirai *et al.*, 2006; Masui *et al.*, 2006; Pencer *et al.*, 2006*a*), to the best of our knowledge the theory presented here constitutes the first complete treatment of the laterally heterogeneous vesicle form factor, since the problem was originally posed by Moody (1975).

In this paper, form factors are derived for vesicles containing single circular or annular domains. These models are then used to fit experimental data and extract both the scattering length density (SLD) and area fractions of phases in a two component membrane. A number of issues, such as heterogeneities in SLD perpendicular to the membrane plane, vesicle polydispersity, the validity of the thin-shell approximation, and the relevance and applicability of the scattering models, are also discussed.

2. Theory

Here, we use a slightly different notation from that of Pencer *et al.* (2006*a*). For convenience of discussion, in lieu of the coherent scattering length density, $\rho(\mathbf{r})$, we use the macroscopic optical potential, $U(\mathbf{r})$, where the two are related by (Sears, 1989)

$$U(\mathbf{r}) = \frac{2\pi\hbar^2\rho(\mathbf{r})}{m}. \tag{1}$$

where m is the neutron mass, $\mathbf{r}$ is the vector from the origin, and $\hbar = h/2\pi$, where h is Planck's constant. The potential U will be expanded in spherical harmonics in a convenient frame of reference for $\mathbf{r}$. In the discussion below, we will show two expansions of $U(\mathbf{r})$.

The Born approximation can be written as

$$\mathrm{d}\sigma = \frac{m^2}{4\pi^2h^4}\left|\int U(\mathbf{r})\exp(-i\mathbf{q}\cdot\mathbf{r})\,\mathrm{d}^3\mathbf{r}\right|^2, \tag{2}$$

where $|\mathbf{q}| = 4\pi\sin(\theta/2)/\lambda$ (θ is the scattering angle, λ is the wavelength), and $\mathbf{q}$ points from the origin to the detector. The amplitude of the approximation is

$$a = -\frac{m}{2\pi h^2}\int U(\mathbf{r})\exp(-i\mathbf{q}\cdot\mathbf{r})\,\mathrm{d}^3\mathbf{r}. \tag{3}$$

The symmetry of the problem at hand is defined by the spherical vesicle shell, which we define in spherical coordinates as

$$v_l^m(r) = \int U(\mathbf{r})Y_l^{m*}(\hat{\mathbf{r}})\sin\theta\,\mathrm{d}\theta\,\mathrm{d}\varphi. \tag{4}$$

Note that $\hat{\boldsymbol{q}}$ and $\hat{\boldsymbol{r}}$ are unit vectors whose directions are parallel to $\mathbf{q}$ and $\mathbf{r}$, respectively. The expansion of the plane wave $\exp(-i\mathbf{q}\cdot\mathbf{r})$ in terms of spherical harmonics, Y_l^m, is given by (Newton, 2002)

$$\exp(-i\mathbf{q}\cdot\mathbf{r}) = \frac{4\pi}{qr}\sum_{l,m}(-i)^l u_l(qr)Y_l^{m*}(\hat{\mathbf{r}})Y_l^m(\hat{\boldsymbol{q}}) \tag{5}$$

$$= 4\pi\sum_{l,m}(-i)^l j_l(qr)Y_l^{m*}(\hat{\mathbf{r}})Y_l^m(\hat{\boldsymbol{q}}). \tag{6}$$

The two functions are put together and integrated, resulting in

$$a(\mathbf{q}) = -\frac{m}{2\pi h^2}\int U(\mathbf{r})\exp(-i\mathbf{q}\cdot\mathbf{r})\,\mathrm{d}^3\mathbf{r}$$

$$= -\frac{2m}{h^2}\sum_{l,m}(-i)^l Y_l^m(\hat{\boldsymbol{q}})\int_0^\infty r^2 j_l(qr)v_l^m(r)\,\mathrm{d}r, \tag{7}$$

where j_l are spherical Bessel functions of order l (Newton, 2002).

For heterogeneous vesicles (*e.g.* shown schematically in Fig. 1), we expand the potential U into two contributions: W, which is homogeneous with respect to θ and φ, and V, which is heterogeneous with respect to θ and φ. Suppose that the raft phase on a vesicle has an SLD ρ_1, and covers a relative vesicle area a_1, and that the remaining vesicle has an SLD ρ_2, and covers a relative area a_2. If the vesicle is heated until its

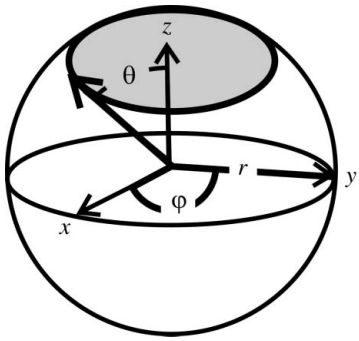

Figure 1
Schematic of a heterogeneous vesicle. The circle defined by the angle θ defines a circular domain, centred on the z axis, of a vesicle of radius r.

components are homogeneously mixed, the vesicle should have an SLD $\bar{\rho}(r) = a_1\rho_1(r) + a_2\rho_2(r)$. This leads to two possible definitions for V and W.

If we take the homogeneous part of U to correspond to the contribution from the average SLD, then

$$W(\mathbf{r}) = W(r) = \bar{\rho}(r) = a_1\rho_1(r) + a_2\rho_2(r) \tag{8}$$

for all values of θ and φ, and

$$V(\mathbf{r}) = \rho(r, \theta, \varphi), \tag{9}$$

where $\rho(r, \theta, \varphi) = \rho_1(r)$ inside the raft phase and $\rho(r, \theta, \varphi) = \rho_2(r)$ outside the raft phase. Alternatively, we can take the homogeneous contribution to U to correspond to the majority phase. In this case,

$$W(\mathbf{r}) = W(r) = \rho_2(r), \tag{10}$$

for all values of θ and φ, and

$$V(\mathbf{r}) = \rho(r, \theta, \varphi), \tag{11}$$

where $\rho(r, \theta, \varphi) = \rho_1(r, \theta, \varphi) - \rho_2(r)$ inside the raft phase and $\rho(r, \theta, \varphi) = 0$ outside. In the following derivation for the heterogeneous vesicle form factor, we will use the latter definitions [*e.g.* equations (10) and (11)] of $V(\mathbf{r})$ and $W(\mathbf{r})$.

Two further simplifications can be made to this model. The first is to assume that the SLD is factorizable into radial and angular components, while the second is to assume that the boundary between phases is sharp. Below, we will also include a further simplification that the SLD is constant with respect to θ and φ inside each phase. The results below can be generalized, however, to cases where the SLD is variable within the phases.

While it is possible to obtain laterally homogeneous membranes, either by restricting membrane components to ones that are fully miscible or by working under the appropriate experimental conditions, such membranes can still be heterogeneous perpendicular to the membrane plane, in particular because the lipid acyl chains and lipid head-groups are chemically distinct. The correct form of $\rho_{\rm radial}(r)$ should therefore take into account such heterogeneities. A further complication is the possible mismatch between the thickness of the rafts and the remaining vesicle, which can be taken care of by the appropriate definitions of both the radial SLD, $v_{\rm radial}(r)$ and a transition zone, given by $w_{\rm angular}(\theta, \varphi)$.

2.1. The heterogeneous vesicle form factor

Below, we consider the case of a single domain (or raft) as a circle on the surface of a sphere. In the Appendices, we generalize these results to more complicated domains. For the calculation presented here, it is convenient to consider the coordinate system having the z axis pointing through the centre of this circle, and α, as the angle between the z axis and the conic surface, centred on the vesicle centre and supported on the boundary of the raft. The contribution from the raft to the scattering amplitude can be evaluated through a simplification of the above formula,

$$\int V(\mathbf{r}) \exp(-i\mathbf{q}\cdot\mathbf{r})\,\mathrm{d}^3\mathbf{r} = 4\pi \sum_l (-i)^l Y_l^0(\hat{\boldsymbol{q}}) \int_0^\infty V(r\hat{\boldsymbol{r}}) r^2 j_l(qr) Y_l^0(\hat{\boldsymbol{r}})\,\mathrm{d}r. \tag{12}$$

For the normalization we use

$$Y_l^0(\theta, \varphi) = i^l \left(\frac{2l+1}{4\pi}\right)^{1/2} P_l(\cos\theta), \tag{13}$$

where P_l are Legendre polynomials of order l (Newton, 2002).

As a first simplification, we assume that the raft contribution can be factored into a radial dependent term, v, and an angular dependent term, w,

$$V(r\hat{\boldsymbol{r}}) = v(r) w(\hat{\boldsymbol{r}}). \tag{14}$$

Then, the raft contribution is

$$\int V(\mathbf{r}) \exp(-i\mathbf{q}\cdot\mathbf{r})\,\mathrm{d}^3\mathbf{r} = \sum_l (2l+1) P_l\big(\cos\theta_q\big) \times \int_0^\infty v(r) r^2 j_l(qr)\,\mathrm{d}r \int_0^\alpha w(\cos\theta) P_l(\cos\theta) \sin\theta\,\mathrm{d}\theta, \tag{15}$$

where θ_q is the angle between the z axis and the scattering vector $\mathbf{q}$. Note that since the raft is circular and centred on the z-axis, there is no dependence of w on φ.

For convenience, we define the following functions,

$$X_l(\alpha) = \int_0^\alpha w(\cos\theta) P_l(\cos\theta) \sin\theta\,\mathrm{d}\theta \tag{16}$$

and

$$Z_l(q, R) = q \int_0^\infty v(r) r^2 j_l(qr)\,\mathrm{d}r. \tag{17}$$

We can then rewrite the raft contribution as

$$\int V(\mathbf{r}) \exp(-i\mathbf{q}\cdot\mathbf{r})\,\mathrm{d}^3\mathbf{r} = \frac{1}{q} \sum_l (2l+1) P_l\big(\cos\theta_q\big) \times X_l(\alpha) Z_l(q, R). \tag{18}$$

As will be shown, the radial and angular integration parts can be processed further.

For a single raft on a vesicle, the combined contributions from the raft and vesicle can be written as

$$\int U(\mathbf{r})\exp(-i\mathbf{q}\cdot\mathbf{r})\,\mathrm{d}^3\mathbf{r} = \frac{2}{q}Z_W(q,R) + \frac{1}{q}Z_0(q,R)X_0(\alpha) + \frac{1}{q}\sum_{l=1}^{\infty}(2l+1)P_l(\cos\theta_q)Z_l(q,R)X_l(\alpha), \tag{19}$$

where $Z_W(q,R)$ is the homogeneous vesicle contribution, defined as

$$Z_W(q,R) = q\int_0^{\infty} W(r)r^2 j_0(qr)\,\mathrm{d}r. \tag{20}$$

If one assumes that the vector $\hat{\boldsymbol{q}}$ is randomly distributed, and one applies the formula for the integrated cross section given by Harrison (1969),

$$\int F(\mathbf{q})F^*(\mathbf{q})\,\mathrm{d}\hat{\boldsymbol{q}}, \tag{21}$$

one obtains

$$\frac{1}{2}\int\left[\int U(\mathbf{r})\exp(-i\mathbf{q}\cdot\mathbf{r})\,\mathrm{d}^3\mathbf{r}\right]^2\sin\theta_q\,\mathrm{d}\theta_q = \left\{\frac{2Z_W(q,R)+Z_0(q,R)X_0(\alpha)}{q}\right\}^2 + \frac{1}{q^2}\sum_{l=1}^{\infty}(2l+1)^2Z_l^2(q,R)X_l^2(\alpha). \tag{22}$$

Note that the first term is the only one that contains both the contribution from the dominant component of the vesicle wall and the contribution from the raft. Note also that, to first order, in the raft contribution one can only see a constant factor multiplying the original interference pattern. Any change to the pattern is of second order and results from the raft's self-correlation function. This result applies to any laterally heterogeneous vesicle that shows cylindrical symmetry. Below, we determine both the angular and radial factors, $X_l(\cos\alpha)$ and $Z_l(q,R)$, respectively, for specific forms of $v(r)$ and $w(\cos\theta)$, in particular for a vesicle with a single circular domain.

2.1.1. The angular factors. As discussed previously, we assume that the boundary between the raft and the surrounding membrane is sharp. Moreover, the SLD within the raft region does not vary with θ or φ. The angular SLD term, $w(\cos\theta)$, can then be written as

$$w(\cos\theta) = 1 \quad \text{for} \quad 0 \le \theta \le \alpha, \tag{23}$$

$$w(\cos\theta) = 0 \quad \text{for} \quad \theta > \alpha. \tag{24}$$

To compute the angular factor $X_l(\alpha)$, we start from the relation given by Lebedev (1972),

$$P'_{l+1}(x) - xP'_l(x) = (l+1)P_l(x). \tag{25}$$

A slight rearrangement then gives

$$P'_{l+1}(x) - (xP_l)'(x) = lP_l(x). \tag{26}$$

This equation is then integrated and used in the computation of $X_l(\alpha)$,

$$l\int_{\cos\alpha}^{1} P_l(x)\,\mathrm{d}x = \left[P_{l+1}(x) - xP_l(x)\right]\Big|_{\cos\alpha}^{1}. \tag{27}$$

Rearranging, one obtains for $X_l(\alpha)$ and $l > 0$,

$$X_l(\alpha) = \int_{\cos\alpha}^{1} P_l(x)\,\mathrm{d}x = \frac{\cos\alpha P_l(\cos\alpha) - P_{l+1}(\cos\alpha)}{l}. \tag{28}$$

$X_0(\alpha)$ is computed directly by

$$X_0(\alpha) = 1 - \cos\alpha. \tag{29}$$

For $l \ll R_{\mathrm{vesicle}}/R_{\mathrm{raft}}$, one can estimate the angular factor for small rafts by

$$X_l(\alpha) \simeq (1 - \cos\alpha). \tag{30}$$

2.1.2. The radial factors. The lipid membrane of a vesicle typically has a radially heterogeneous SLD profile, even if it is laterally homogeneous, resulting from the differences in SLD between the lipid head-group and acyl-chain regions. Models for radially heterogeneous lipid membranes are discussed in detail by *e.g.* Kučerka *et al.* (2004) and Pencer *et al.* (2006). However, as discussed by Pencer *et al.* (2006*a*), it is experimentally possible to produce vesicles with radially homogeneous SLD through the partial deuteration of the lipid acyl chains. Below we consider two possibilities for $v(r)$: (i) radially homogeneous membranes, and (ii) membranes with three uniform layers, corresponding to the inner and outer head-group regions and acyl-chain region.

For radially homogeneous membranes [case (i)], $v(r)$ is given by

$$v(r) = \begin{cases} \rho(r) & \text{for } R_{\mathrm{i}} \le r \le R_{\mathrm{o}} \\ 0 & \text{for } r < R_{\mathrm{i}},\ r > R_{\mathrm{o}}, \end{cases} \tag{31}$$

where ρ is the mean SLD of the membrane, and R_{i} and R_{o} are the vesicle inner and outer radii, respectively.

In evaluating $Z_l(q,R)$, we first consider case (i). As discussed by Pencer *et al.* (2006*a*), this case corresponds experimentally to the situation where the mean acyl-chain SLD equals that of the lipid head-group region. The calculation of $Z_W(q,R)$ using $W(r) = \rho_2(r)$ is equivalent to that of $Z_0(q,R)$ using $v(r) = \rho(r)$. $Z_l(q,R)$ in some cases can be computed using only elementary transcendental functions, while in other cases is calculated using the integral sine and cosine functions. $Z_l(q,R)$ for $l = 0, 1, 2$, will be computed first. This is done for two purposes: first, the zeroth-order term is compared with known results (Kerker, 1969) and, second, that in some cases the zeroth-, first- and second-order terms are all that are needed. The functions

$$j_0 = \frac{\sin z}{z},$$
$$j_1 = -\frac{\cos z}{z} + \frac{\sin z}{z^2}, \quad (32)$$
$$j_2 = -3\frac{\cos z}{z^2} + \left(\frac{3}{z^2} - 1\right)\frac{\sin z}{z},$$

are integrated between R_i and R_o (as defined by Pencer & Hallett, 2003). The results are

$$Z_0(q, R) = \rho\left[r^2\left(\frac{\sin qr}{(qr)^2} - \frac{\cos qr}{qr}\right)\right]\Bigg|_{R_\mathrm{i}}^{R_\mathrm{o}},$$
$$Z_1(q, R) = \rho\left[r^2\left(-\frac{2\cos qr}{(qr)^2} - \frac{\sin qr}{qr}\right)\right]\Bigg|_{R_\mathrm{i}}^{R_\mathrm{o}}, \quad (33)$$
$$Z_2(q, R) = \rho\left[r^2\left(-\frac{4\sin qr}{(qr)^2} + \frac{\cos qr}{qr} + \frac{3\mathrm{Si}(qr)}{(qr)^2}\right)\right]\Bigg|_{R_\mathrm{i}}^{R_\mathrm{o}},$$

where

$$\mathrm{Si}(z) = \int_0^z \frac{\sin y}{y}\,\mathrm{d}y.$$

Rearranging the terms, and changing the function definitions accordingly, one can see that the formula for Z_0 is similar to the term derived by Pencer & Hallett (2003).

Using the definitions of Newton (2002) and McLachlan (1955), we can define j_l as

$$j_l = (-1)^l z^l \left(\frac{1}{z}\frac{\mathrm{d}}{\mathrm{d}z}\right)^l [j_0(z)]. \quad (34)$$

Z_l are computed according to equation (17). Changing the variable to $z = qr$ yields

$$Z_l(q, R) = \frac{\rho}{q^2}\int_{qR_\mathrm{i}}^{qR_\mathrm{o}} j_l(z) z^2\,\mathrm{d}z. \quad (35)$$

If one assumes that the vesicle is thin, then the radial integration reduces to a product,

$$Z_l(q, R) \simeq \rho q j_l\left(\frac{qR_\mathrm{o} + qR_\mathrm{i}}{2}\right)(R_\mathrm{o} - R_\mathrm{i})\left(\frac{R_\mathrm{o} + R_\mathrm{i}}{2}\right)^2. \quad (36)$$

For radially heterogeneous vesicles, case (ii), the form for Z_l remains the same as in case (i); however, the limits of integration change. To account for the differences between the lipid acyl-chain and head-group regions [case (ii)], $\rho(r)$ is given by

$$\rho(r) = \begin{cases} \rho_\mathrm{h} & \text{for} \quad R_0 \le r \le R_1 \\ \rho_\mathrm{ac} & \text{for} \quad R_1 < r < R_2 \\ \rho_\mathrm{h} & \text{for} \quad R_2 \le r \le R_3 \\ 0 & \text{for} \quad r < R_0,\ r > R_3. \end{cases} \quad (37)$$

The functions j_l are then evaluated between R_0 and R_3. For $Z_0(q, R)$ this gives

Table 1
Parameters extracted from the DLPC:DPPC phase diagram of van Dijck *et al.* (1977).

Subscript 1 denotes the solid (gel) phase and subscript 2 denotes the liquid (fluid) phase.

Molar fraction of DPPC in solid phase, X_1	0.85
Molar fraction of DPPC in liquid phase, X_2	0.34
Relative molar fraction of solid phase, n_1	0.31
Relative molar fraction of liquid phase, n_2	0.69

$$Z_0(q, R) = \sum_{N=1}^{3} \rho_N\left[r^2\left(\frac{\sin qr}{(qr)^2} - \frac{\cos qr}{qr}\right)\right]\Bigg|_{R_{N-1}}^{R_N}, \quad (38)$$

where Z_l are evaluated similarly to Z_0, $\rho_1 = \rho_3 = \rho_\mathrm{h}$ and $\rho_2 = \rho_\mathrm{ac}$, and R_N are as above.

Using the derived form factors, it is also possible to evaluate a number of other cases for laterally heterogeneous vesicles. In the Appendices, we consider three cases: Appendix *A* describes the form factor for circular domains on the inner and outer monolayers formed independently, while Appendix *B* describes the form factor for single annular domains.

3. Evaluation of the model

Below, scattering curves are calculated for mixed lipid vesicles exhibiting lateral heterogeneities. The calculations and plots that follow will be used to assess several approximations to the form factor.

3.1. Structural parameters

To generate data relevant to experimental conditions, we use compositions and area fractions derived from the phase diagram for mixtures of 1,2-dipalmitoyl-sn-*glycero*-3-phosphocholine (DPPC) and 1,2-dilauroyl-sn-*glycero*-3-phosphocholine (DLPC) (van Dijck *et al.*, 1977). The experimental data, which will be discussed in a subsequent section, has also been obtained for this lipid mixture. In Table 1, the relative fractions of DPPC in the liquid and solid phases are given, as well as the relative molar fraction of each phase. Accurate determination of the volume fractions and SLD of the solid and fluid phases requires knowledge of the molecular volumes of DPPC and DLPC in each phase. Alternatively, we can assume that the lipid molecular volumes are equal to each other, and equal in both the solid and liquid phases. We will test the accuracy of this assumption below.

In order to calculate the relative volume fractions of the solid and liquid phases, we use the molecular volumes of pure DPPC and DLPC in their respective phases; *i.e.* the volume of DPPC in the solid phase will equal that of pure DPPC in its gel phase, and so on. We can then calculate the relative volume fraction of the gel phase (denoted by the subscript 1), v_1, as

$$v_1 = \frac{n_1\left[X_2 V_{1,1} + (1 - X_2)V_{1,2}\right]}{n_1\left[X_2 V_{1,1} + (1 - X_2)V_{1,2}\right] + n_2\left[X_2 V_{2,1} + (1 - X_2)V_{2,2}\right]}, \quad (39)$$

where $V_{i,1}$, $V_{i,2}$, are the molecular volumes of DPPC (1) and DLPC (2) in the gel ($i = 1$) and liquid ($i = 2$) phases, respectively. We use volumes of 1144 and 1232 Å^3 for DPPC in the gel and liquid phases, respectively (Nagle & Tristram-Nagle, 2000), 991 Å^3 for DLPC in the fluid phase (Kučerka *et al.*, 2005) and estimate a volume of 910 Å^3 for DLPC in the gel phase. We find that the relative volume fractions of the gel and fluid phases are 0.32 and 0.68, respectively. Note that, if the molecular volumes of DPPC and DLPC were assumed to be the same in both phases, then the relative volume fractions would be 0.31 and 0.69.

The SLD of the gel and fluid phases is determined *via* (Pencer *et al.*, 2005)

$$\rho_1 = \frac{n_{1,1}V_{1,1}\rho_{1,1} + n_{1,2}V_{1,2}\rho_{1,2}}{n_{1,1}V_{1,1} + n_{1,2}V_{1,2}}, \qquad (40)$$

where $n_{1,i}$, $V_{1,i}$ and $\rho_{1,i}$ are the number, molecular volume and SLD of lipids of species i in region 1. The total volume of region 1 is $V_1 = n_{1,1}V_{1,1} + n_{1,2}V_{1,2}$. Note that our modelling requires separate determinations of the head-group and acyl-chain SLD. Following the arguments of Nagle & Tristram-Nagle (2000), we assume a constant molecular volume of 319 Å^3 for the phosphocholine head-group for both DLPC and DPPC, regardless of phase. We obtain an SLD of 1.88×10^{-6} Å^{-2} for the head-group region, 1.08×10^{-6} Å^{-2} for the acyl-chain region of the fluid phase, and 3.07×10^{-6} Å^{-2} for the gel phase. The mean membrane SLD and mean acyl-chain SLD in the fluid phase are 1.73×10^{-6} Å^{-2} and 1.67×10^{-6} Å^{-2}, respectively.

Finally, we consider differences in the thickness and molecular areas of lipids in the gel and fluid phases. On heating from the gel to liquid phase, DPPC shows a decrease in thickness of ~6 Å (17%) and concomitant increase in area of roughly 15 Å^2 (30%) (Nagle & Tristram-Nagle, 2000). These differences provide an upper bound on our estimates of the differences between mean molecular thickness and areas of lipids in the gel and fluid phases of the DLPC–DPPC mixture. If we assume the maximum difference between mean molecular areas in the gel and fluid phases of 30%, then a molar fraction of 0.69 for the fluid phase translates to an area fraction of 0.74. Table 2 summarizes the parameters used to generate the scattering curves that follow.

3.2. Polydispersity

In practice, ULVs are always polydisperse. In order to account for polydispersity, the vesicle scattering function is integrated with the size distribution, $G(R)$, either numerically (*e.g.*, Pencer & Hallett, 2003; Kučerka *et al.*, 2004) or analytically, by assuming a uniform membrane SLD and a Schultz distribution for $G(R)$ (*e.g.* Aragòn & Pecora, 1976). We have recently shown that, using the separated form factor (SFF) approximation (Kiselev *et al.*, 2002), the procedure of Aragòn & Pecora (1976) can be generalized to polydisperse ULVs of arbitrary membrane SLD (Pencer *et al.*, 2006). In Appendix *C* we further extend our previous results to provide expressions for arbitrary Z_l in the case of polydisperse vesicles.

Table 2
Mean membrane SLD ($\bar{\rho}$), mean acyl-chain SLD (ρ_{ac}) and mean head-group SLD (ρ_h) for a 1:1 mixture of DLPC:DPPC at 298 K.

The lipid mixture contains 0.5 molar fractions of DPPC and chain perdeuterated DPPC (dDPPC).

Mean vesicle radius, R (Å)	300
Vesicle relative polydispersity, $\sigma/\langle R\rangle$	0.25
Head-group thickness, t_h (Å)	10
Gel-phase acyl-chain thickness, $t_{ac,1}$ (Å)	36
Liquid-phase acyl-chain thickness, $t_{ac,2}$ (Å)	30
Relative volume fraction of gel phase, v_1	0.32
Relative volume fraction of liquid phase, v_2	0.68
Relative area fraction of gel phase, a_1	0.26
Relative area fraction of liquid phase, a_2	0.74
Mean membrane SLD, $\bar{\rho}$ (Å^{-2})	1.73×10^{-6}
Mean acyl-chain SLD, ρ_{ac} (Å^{-2})	1.67×10^{-6}
Head-group SLD, ρ_h (Å^{-2})	1.88×10^{-6}
Acyl-chain SLD of solid phase, $\rho_{ac,1}$ (Å^{-2})	3.07×10^{-6}
Acyl-chain SLD of liquid phase, $\rho_{ac,2}$ (Å^{-2})	1.08×10^{-6}
SLD of medium, ρ_s (Å^{-2})	1.73×10^{-6}

3.3. Truncation effects in the series representation

Calculation of the scattering function for heterogeneous vesicles relies on a series representation. For practical purposes, it is therefore important to determine how many orders of the series expansion are required to reasonably fit the data. In this regard, two factors are important: the magnitude of the angular factors, $X_l(\alpha)$, and the radial factors, $Z_l(q, R)$, as a function of order l.

Fig. 2 shows $X_l(\alpha)$, plotted as a function of order l for several domain sizes, α, ranging from 30 to 150°, corresponding to a total ULV surface area fraction of between 7 and 93%. For all values of α, the magnitude of $X_l(\alpha)$ decreases as l increases, and is significantly more rapid for large domains. In particular, for large domains ($\alpha \simeq 150°$) $X_6(\alpha)$ is less than 1% of $X_0(\alpha)$, while for small domains ($\alpha \simeq 30°$) the relative contribution of $X_6(\alpha)$ is ~10%.

In Fig. 3, $Z_l(q, R)$ (using the SFF approximation) are plotted as a function of scattering vector, q, for orders $l = 0$ to 5. It is noteworthy that the only non-zero $Z_l(q, R)$ at $q = 0$ is the zeroth-order radial factor, which is equivalent to the scattering

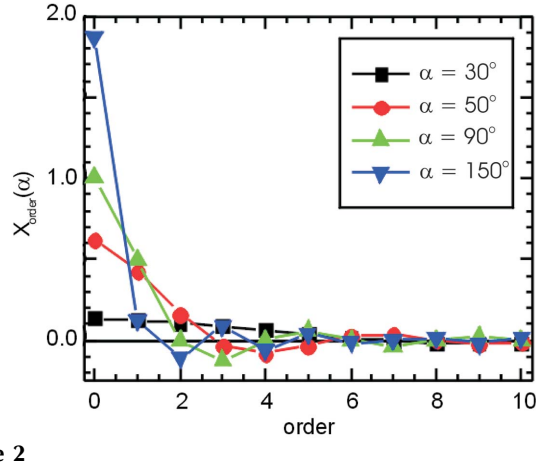

Figure 2
The angular factors, $X_l(\alpha)$, plotted as a function of order, l, for several values of domain size, α.

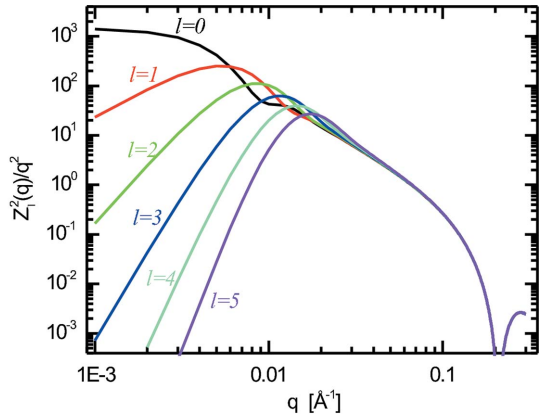

Figure 3
The radial factors, $Z_l(q, R)$, plotted as a function of the modulus of the scattering vector value, q. The mean vesicle radius is R = 300 Å, and polydispersity is $\sigma/\langle R\rangle$ = 0.25. The curves are calculated using the separated form-factor approximation (*i.e.* $t < R$).

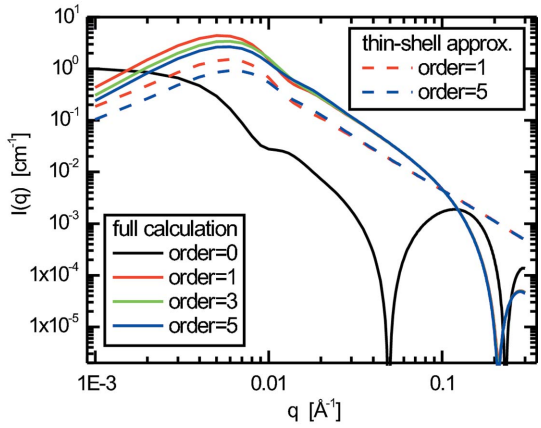

Figure 4
Calculated scattering curves for polydisperse heterogeneous vesicles. The parameters used for the calculation are summarized in Table 1.

contribution from homogeneous vesicles. The higher order $Z_l(q, R)$ show maxima at intermediate length scales, which decrease in value and are shifted to higher q as the order l increases. As the order l increases, the relative contribution of $Z_l(q, R)X_l(\alpha)$ rapidly decreases.

Finally, Fig. 4 shows plots of the full form factor for heterogeneous vesicles as a function of q, plotted for $l = 0$ to 5. Clearly, the most dramatic change in the scattering curves occurs between $l = 0$ and $l = 1$. This change corresponds to the addition of the leading order 'non-homogeneous' term to the homogeneous form factor ($l = 0$). The addition of higher order terms produces only small qualitative changes to the scattering curve. Thus, the primary influence of heterogeneity on the q-dependence of the scattering curve is essentially captured by the addition of the $l = 1$ term alone. It seems, therefore, that the scattering function is reasonably insensitive to truncation of higher order terms in its expansion.

3.4. The thin-shell approximation

Thus far, we have discussed the importance of $l > 0$ terms in the expansion of the heterogeneous vesicle form factor. Also of interest is the potential contribution of the bilayer membrane form factor (or radial SLD profile) to the vesicle form factor. Fig. 4 shows calculations for the 'thin shell' form factor (for $l = 1$ and $l = 5$) using the parameters from Table 1. In this case, we assume that the radial density is a delta function in r. Comparison of these curves with the full scattering curves shows that the thin shell approximation follows the full function up to about q = 0.05 Å^{-1}, or $qt \simeq 2.5$. It is likely that the thin shell approximation for heterogeneous vesicles is most robust for $qt < 1$; however, we have not investigated this in detail.

3.5. Validity of the analytic models

SANS measurements on a vesicle sample yield data averaged over time, vesicle orientation and a large number of vesicles. Correct interpretation and analysis of SANS from heterogeneous vesicles therefore requires that domains are stable over the course of the measurement, and that orientational and ensemble averaging is taken into account when calculating the form factor. In particular, the analytic models that we have derived implicitly assume that all vesicles in a sample show the same type and relative size of domain and that these domains do not change as a function of time. Limitations of this approach are: (*a*) if there is variation in the size and morphology of domains among vesicles, the analysis will provide an intensity averaged representation, and (*b*) if domains grow or disappear as a function of time, the apparent domain size will depend on the time interval of the measurements.

In the case of heterogeneous GUV showing liquid–liquid phase coexistence, it has recently been demonstrated that domain coarsening or coalescence occurs within minutes, resulting in single circular domains in each vesicle (Yanagisawa *et al.*, 2007). While in some cases 'trapped coarsening' or the metastability of multiple domains can occur, we do not expect such behaviour here; our samples are prepared in the absence of solute or buffer, allowing vesicles to maintain a spherical shape (see *e.g.* Pencer *et al.*, 2001), while the process of 'trapped coarsening' has been shown to depend on the availability of excess area, maintained by an osmotic gradient (Yanagisawa *et al.*, 2007). Thus, we expect both domain stability and uniformity among vesicles. However, we cannot discount the possibility of domain morphologies beyond those considered here. We will return to a discussion of this in the conclusion (§6).

3.6. The detection limit for membrane domains

As discussed above, selective deuteration of one of the lipid components present is required to obtain the contrast necessary to distinguish between membrane domains and the remaining vesicle. However, even under optimal contrast conditions there is a minimum detectable domain size. Evaluation of this lower bound on domain size requires a reexamination of the heterogeneous vesicle form factor [equation (22)]. Note that, under optimal contrast matching conditions (SLD head-group = SLD medium = mean acyl-

chain SLD), the first term in equation (22) does not contribute to the scattered intensity. Consequently, the scattered intensity from heterogeneous vesicles will be proportional to $X_1(\alpha)Z_1(qR)$ plus higher order terms. For the special case of circular domains, we find that

$$I \propto (\rho_1 - \rho_2)^2[\cos(\alpha)P_1(\cos\alpha) - P_2(\cos\alpha)]^2,$$
$$\propto \frac{1}{4}(\rho_1 - \rho_2)^2 \sin^4\alpha, \quad (41)$$

where ρ_1 and ρ_2 are the SLD of the domain and remaining vesicle, and α is the angle defined by the lines from the origin (centre of the vesicle) to the domain centre and its edge. Thus the absolute detection limit will depend not only on the domain size (defined by α) but also on the domain–vesicle contrast ($\rho_1 - \rho_2$).

Suppose that, in order to detect domains, we require at least 1% of the maximum possible intensity due to the domain–vesicle contrast. This 1% signal will require an angle, α, of at least 0.1π or approximately 20°, corresponding to an area fraction on the vesicle surface of about 3%. For a 30 nm-radius vesicle, the minimum detectable domain size would therefore be approximately 10 nm in radius (note that, since the domain is projected onto a spherical surface, a domain covering half the vesicle surface would have a radius of 60 nm).

4. Experimental procedures

4.1. Materials

1,2-Dipalmitoyl-sn-*glycero*-3-phosphocholine (DPPC), 1,2-dipalmitoyl-D62-sn-*glycero*-3-phosphocholine (dDPPC), and 1,2-dilauroyl-sn-*glycero*-3-phosphocholine (DLPC) were purchased from Avanti Polar Lipids (Birmingham, AL, USA) as lyophilized powders, and used without further purification. Upon arrival, the various lipids were stored at 233 K. 99% purity D_2O was purchased from Cambridge Scientific (Andover, MA, USA), while all other chemicals were reagent grade.

4.2. Vesicle preparation

Lipids solubilized in chloroform were transferred to 4 ml glass vials in appropriate proportions to produce solubilized lipid mixtures of predetermined molar ratios. The chloroform was removed under a stream of N_2 followed by vacuum pumping. Lipid films were then preheated to 333 K and dispersed, by agitation, using deionized water that was filtered through a Millipore Milli-Q water purification system (mixed in appropriate D_2O ratios), which had also been preheated to 333 K. The lipid dispersions were then extruded using a hand-held extruder (Avanti Polar Lipids), preheated to 333 K. Total lipid concentrations ranged from 1 to 10 mg ml^{-1}. ULVs with approximately 30 nm radius were formed by successive extrusions using polycarbonate filters with three different pore diameters, and a total of 43 passes [*e.g.* 200 nm (9 times), 100 nm (9 times) and 50 nm (25 times)].

4.3. Contrast matching

The detection of membrane domains by SANS requires the deuteration of at least one membrane component. Here, the DPPC component in DPPC–DLPC mixtures was chain deuterated, in order to enhance the contrast between DPPC-rich and DPPC-depleted domains. Optimal contrast conditions for detection of lateral heterogeneities in membranes also relies on contrast matching the homogeneously mixed components. The calculation of the mean vesicle SLD and corresponding contrast match point is described in detail by Pencer *et al.* (2005). As discussed by Pencer *et al.* (2006*a*) it is advantageous to work under conditions where the lipid head-group region is also contrast matched. Lipid and component SLD are determined using known atomic scattering lengths (Sears, 1992), and molecular and component volumes (Nagle & Tristram-Nagle, 2000; Kučerka *et al.*, 2005). In a 1:1 DPPC–DLPC mixture, chain deuteration of 57 mol% of the DPPC lipid fraction gives a mean acyl-chain region SLD of $\sim$2.0 $\times$ 10^{-6} Å^{-2}, close to that of the lipid head-group region ($\sim$1.8 $\times$ 10^{-6} Å^{-2}). Dispersion of lipids in 36 mol% D_2O ($\sim$2.0 $\times$ 10^{-6} Å^{-2}) yields contrast matching conditions of the mean lipid SLD.

4.4. Small-angle neutron scattering

SANS measurements were performed using the 30 m NG7 instrument (Glinka *et al.*, 1998) located at NIST (Gaithersburg, MD). For sample-to-detector distances (SDD) of 1, 4 and 10 m, 5.5 Å-wavelength (λ) neutrons ($\delta\lambda/\lambda$ = 10%) were used, while 8 Å neutrons were used for a SDD of 12 m. The total range in scattering vector covered was $0.003 < q < 0.5$ Å^{-1}. SANS data were reduced and corrected for sample transmission and background using *IgorPro* (WaveMetrics, Lake Oswego, OR, USA) with subroutines provided by the NIST Center for Neutron Research (NCNR) (Kline, 2006).

Note that, for all samples, data collection times were 20, 10 and 5 min for 12, 4 and 1 m SDD, respectively. Unfortunately, the reduced intensity for samples in 36% D_2O, owing to low contrast, resulted in poor counting statistics in the low-q range. We estimate that between 1 and 2 h of data collection time per sample would be required at 12 m SDD in order to obtain a significant improvement in signal to noise for ULV in 36% D_2O.

4.5. Data analysis

SANS data were analyzed using a non-linear least-squares fitting routine, *MINUIT* (James, 2007), that was linked with the program written by one of the authors (NK). Fitting routines were written in C++ and implemented in the Tcl/Tk environment (http://www.tcl.tk/). During data fitting, parameters could be fixed or loosely constrained using a harmonic potential (Bayesian method). Details of fitting constraints will be discussed in the *Results* section below.

5. Results

5.1. Vesicle characterization

In order to characterize possible changes to vesicle structure due to changes in temperature, scattering functions were measured for ULVs composed of 1:1 mixtures of DPPC and DLPC at 303 and 293 K, using hydrogeneous lipid mixtures in D_2O. Under these contrast conditions, the membrane SLD is essentially laterally homogeneous, even if the lipid lateral distribution is not, as the lipid acyl chains of DLPC and DPPC have essentially the same SLD (-0.38×10^{-6} Å^{-2} and -0.37×10^{-6} Å^{-2}, respectively). Under these contrast conditions, we can expect to measure the vesicle form factor, the heterogeneous radial SLD, and the homogeneous lateral or angular SLD. Scattering curves shown in Fig. 5 are fit well by the form factor for laterally homogeneous vesicles allowing us to determine the vesicle mean size, polydispersity and the thickness of the acyl-chain and head-group regions (Table 3). We find that the vesicle structure remains essentially unchanged on cooling from 303 to 293 K, showing only a 10% decrease in vesicle mean radius and a small increase (∼2 Å) in thickness. As discussed, for laterally heterogeneous vesicles, the membrane thickness may be different in the domain and vesicle regions. If domains are present for DLPC–DPPC ULVs at 293 K, then these results suggest that, for the SANS range examined, the form factor is relatively insensitive to lateral variations in membrane thickness.

5.2. Detecting domains

As discussed by Pencer *et al.* (2006), the optimal contrast conditions to detect membrane domains differ significantly from those required to measure the vesicle form factor. Thus, measurements were also performed to characterize domains in 1:1 mixtures of DPPC and DLPC, with 57 mol% of the DPPC chain deuterated in 36% D_2O. Under these conditions, the scattering contrast is minimized when DPPC and DLPC are homogeneously mixed in the membrane (*i.e.* at high temperature). Cooling the ULV from 303 to 293 K produces lateral segregation, as indicated by the excess scattering signal from the ULV (Fig. 6). This signal arises from the contrast between compositionally distinct ULV domains and the medium.

Table 3
Fitting results for hydrogeneous DPPC:DLPC vesicles.

T (K)	R (Å)	σ (Å)	D_H (Å)	$2D_C$ (Å)
293	277.1 ± 4.3	66.9 ± 2.8	13.1 ± 4.3	18.8 ± 8.6
303	303.2 ± 7.2	79.7 ± 4.3	12.6 ± 4.3	17.8 ± 8.6

5.3. Domain size and SLD

In fitting the data using the various models described above (and in the Appendices), we constrain a number of parameters, based on estimates from known physical quantities. The mean acyl-chain SLD (∼2.0×10^{-6} Å^{-2}) and head-group SLD (∼1.8×10^{-6} Å^{-2}) were calculated from known lipid component volumes and scattering lengths (Nagle & Tristram-Nagle, 2000; Kučerka *et al.*, 2005; Sears, 1992). The head-group and acyl-chain thicknesses were constrained by a harmonic potential to be close to those values found from the fits shown in Fig. 5. We denote the four models used to fit the data as follows: 'cap', corresponding to a single circular domain, 'decoupled caps', corresponding to independent circular

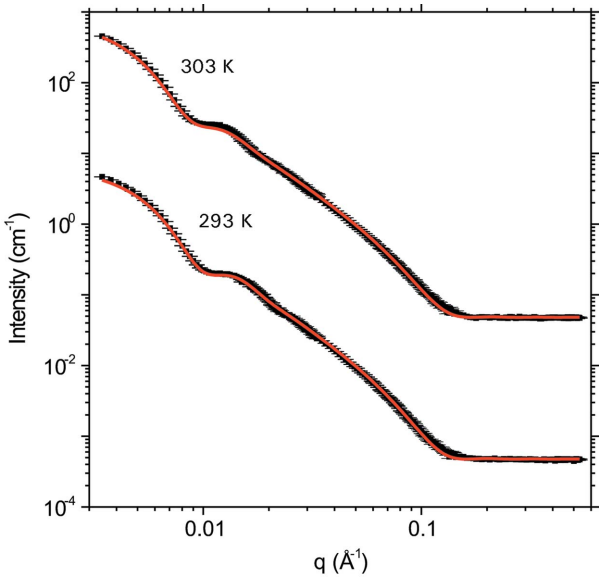

Figure 5
Small-angle neutron scattering from ULVs composed of 1:1 mixtures of DPPC and DLPC taken at 293 (lower curve) and 303 K (upper curve) in 100% D_2O. Symbols correspond to experimental data and solid lines show the fits to the data using the form factor for laterally homogeneous vesicles. The curves have been shifted vertically to facilitate viewing.

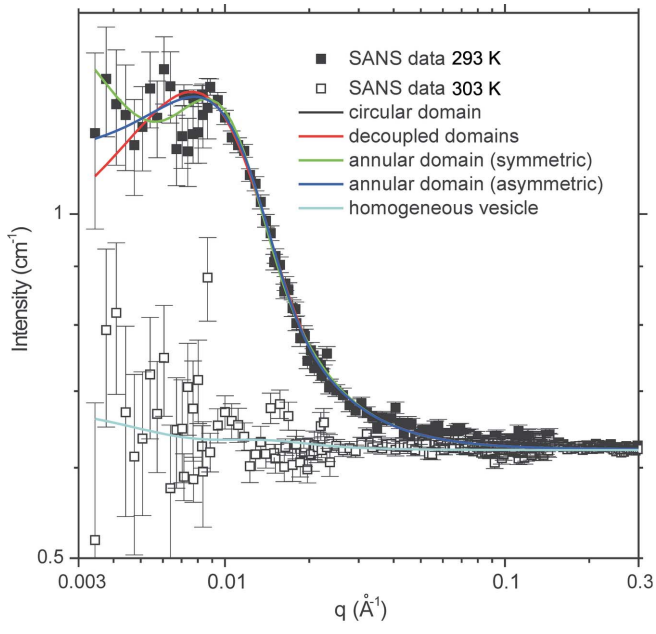

Figure 6
Small-angle neutron scattering from ULVs composed of 1:1 mixtures of DPPC and DLPC. 57 mol% of the total DPPC content corresponds to chain perdeuterated DPPC and the medium was composed of 36% D_2O. Symbols correspond to measurements taken at 293 (upper curve) and 303 K (lower curve) and solid lines are fits to the data.

Table 4
Fitting results for heterogeneous vesicles.

'Model' refers to the various form factors used to fit the data. ρ_v is the acyl-chain SLD of the majority phase (vesicle), ρ_d is the acyl-chain SLD of the minority phase (domain), and a_1 refers to the fraction of total vesicle area occupied by the domain.

Model	ρ_v (Å^{-2})	ρ_d (Å^{-2})	a_1
Cap	$1.8 \pm 0.06 \times 10^{-6}$	$3.4 \pm 0.1 \times 10^{-6}$	0.13 ± 0.01
Decoupled caps	$1.71 \pm 0.08 \times 10^{-6}$	$4.0 \pm 0.1 \times 10^{-6}$	0.13 ± 0.01
Sym annulus	$1.51 \pm 0.05 \times 10^{-6}$	$2.2 \pm 0.1 \times 10^{-6}$	0.23 ± 0.01
Asym annulus	$1.5 \pm 0.1 \times 10^{-6}$	$2.4 \pm 0.1 \times 10^{-6}$	0.44 ± 0.01

domains on the inner and outer membrane monolayers (see Appendix *A*), 'sym annulus', an equatorial annular region bounded by the same angle on the top and bottom (see Appendix *B*), and 'asym annulus', an annular region bounded by different angles on the top and bottom (also described in Appendix *B*). The domain (minority phase) and vesicle (majority phase) SLD, and domain size (a_1) determined from fits using the various models are summarized in Table 4, while the corresponding fits are shown in Fig. 6.

In fitting the data, we find that the 'decoupled caps' model produces a scattering curve that is exactly the same as the 'cap' model. In the case of the 'decoupled caps', however, the fitting produces unphysical results, in particular, a domain acyl-chain SLD greater than that for fully deuterated DPPC. It is also notable that, above $q \simeq 0.01$ Å^{-1}, all four scattering curves superimpose. Because of the relatively poor counting statistics of the data at low q (*i.e.* $q < 0.01$ Å^{-1}), all four models give fits of equivalent quality, despite the different shapes of the scattering curves in this range. Thus, while, on one hand, differences in the form factors of the various models have the potential to uniquely determine the size and shape of domains, on the other hand, such a distinction requires significant data collection time at long SDD.

Interestingly, while all four models give equivalent quality fits to the SANS data over the entire q range obtained, each model provides a different set of parameters for the domain area, a_1 and domain and vesicle SLD. As discussed in §4 and above, longer data collection times are required to obtain the necessary statistics to distinguish between the various models.

5.4. Estimating domain composition

For a two-component mixture that is laterally segregated, the SLD of the two phases can be used to determined the compositions of both phases. Rearranging equation (40) we obtain

$$n_{1,1} = \frac{V_1(\rho_1 - \rho_{1,2})}{V_{1,1}(\rho_{1,1} - \rho_{1,2})}, \quad n_{2,1} = \frac{V_2(\rho_2 - \rho_{2,2})}{V_{2,1}(\rho_{2,1} - \rho_{2,2})},$$
$$n_{1,2} = \frac{V_1(\rho_1 - \rho_{1,1})}{V_{1,2}(\rho_{1,2} - \rho_{1,1})}, \quad n_{2,2} = \frac{V_2(\rho_2 - \rho_{2,1})}{V_{2,2}(\rho_{2,2} - \rho_{2,1})}, \tag{42}$$

where $n_{1,i}$, $V_{1,i}$ and $\rho_{1,i}$ are the number, molecular volume and SLD of lipids of species i in region 1.

The molar fraction of lipids of species 1 in region 1, $x_{1,1}$, and species 1 in region 2, $x_{2,1}$, can then be calculated from

Table 5
Domain and vesicle compositions from fit results.

Model	x_v	x_d
Cap	0.46 ± 0.03	0.80 ± 0.04
Sym annulus	0.39 ± 0.03	0.50 ± 0.03
Asym annulus	0.39 ± 0.03	0.55 ± 0.03

$$x_{1,1} = \frac{n_{1,1}}{n_{1,1} + n_{1,2}} = \frac{V_{1,2}(\rho_1 - \rho_{1,2})}{V_{1,2}(\rho_1 - \rho_{1,2}) - V_{1,1}(\rho_1 - \rho_{1,1})}, \tag{43}$$

and

$$x_{2,1} = \frac{n_{2,1}}{n_{2,1} + n_{2,2}} = \frac{V_{2,2}(\rho_2 - \rho_{2,2})}{V_{2,2}(\rho_2 - \rho_{2,2}) - V_{2,1}(\rho_2 - \rho_{2,1})}, \tag{44}$$

where the parameters $\rho_{1,1}$ and $\rho_{1,2}$ are calculated from the scattering lengths and molecular volumes of lipids of type 1 and 2 in each phase, and ρ_1 is determined from a fit to the data using one of the form factors described here. Known values or estimates for the molecular volumes of DPPC and DLPC in the gel and fluid phases can then be used to calculate the compositions of the domain and vesicle regions. Using the same structural parameters given in §3.1, we calculate domain compositions for the various models, summarized in Table 5.

In Fig. 7, we show a reproduction of the DPPC–DLPC phase diagram, as obtained by van Dijck *et al.* (1977). Note that the phase boundaries have been lowered by 2.5 K to account for the suppression of the transition temperature of deuterated DPPC compared with hydrogeneous DPPC (Katsaras *et al.*, 1997). For any given temperature, the

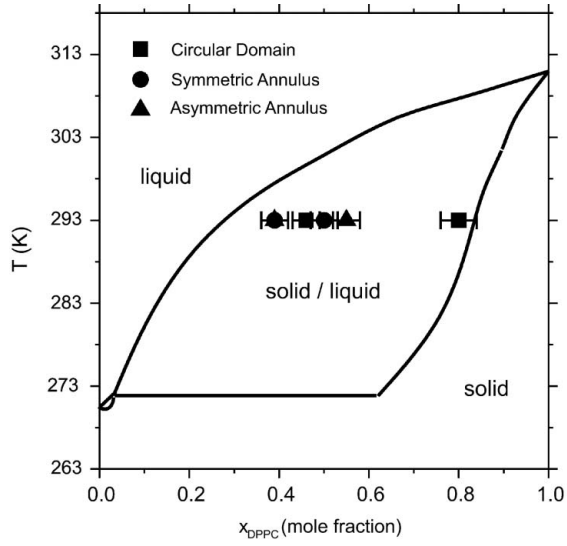

Figure 7
Phase diagram for DPPC–DLPC mixtures (solid lines) adapted from van Dijck *et al.* (1977). Note that, as discussed in the text, the phase boundaries have been shifted by 2.5 K to account for the suppression of the transition temperature of deuterated DPPC as compared with hydrogeneous DPPC. Also shown (solid symbols) are phase boundaries at 293 K determined from the compositions of phases given in Table 4. The boundaries for circular (caps), symmetric annular and asymmetric annular domains are given by solid squares, circles and triangles, respectively.

composition of the liquid and solid phases are given by the boundaries of the solid–liquid coexistence region, on the left and right sides, respectively. Thus, at 293 K we would expect, based on the phase diagram, to find molar fractions of 0.28 and 0.84 in the liquid and solid phases, respectively. For the purpose of comparison, compositions determined from fits to the SANS data are also shown (solid symbols) on the phase diagram.

We find, based on the estimated compositions summarized in Table 5, that the circular domain model gives results that are closest to those expected from the phase diagram. It is worth noting, however, the influence of molecular volume on our calculation of the the domain compositions. If we use the lipid gel phase volumes to calculate the compositions of both regions, we obtain molar fractions of 0.39 and 0.80 in the liquid and solid phases, respectively, while using liquid lipid volumes yields compositions of 0.46 and 0.92 for the liquid and solid phases. Thus, the calculated molar fractions of the phases depend significantly on the initial estimates of molecular volume. Nevertheless, even with ∼10% uncertainties in composition, the circular domain model provides the best agreement with the known phase diagram.

6. Conclusions

We have outlined a general approach to the analytic calculation of form factors for laterally heterogeneous vesicles. We have examined the special case of cylindrically symmetric heterogeneous vesicles and derive specific equations for circular and annular domains. Using the illustrative case of circular domains in a binary mixture, we have shown a number of steps that simplify the application of the heterogeneous form factor, such as truncation of the series representation and the implementation of the separated form factor approach.

Fits to experimental data and comparison among the results from several analytic models show that the circular domain form factor provides the best agreement with predictions from experiment. However, as discussed in the *Introduction*, it is not clear that single circular domains should appear in a solid–liquid mixture. Observations from fluorescence microscopy suggest that DPPC:DLPC mixtures should, in fact, show highly irregular domains. It may be that, under certain conditions, the form factor from vesicles showing a variety of irregular domains resembles that of vesicles with single circular domains. Likewise, membrane curvature (*i.e.* vesicle size) could also play a role in potential differences between the behaviour of giant (micrometre-sized) and the 30 nm-sized vesicles of this study.

In an upcoming study, we intend to perform systematic SANS measurements, as a function of temperature and composition, on binary mixed ULVs. Comparison of SANS results with known phase diagrams will allow us to determine whether the circular domain (or other models) can be effectively used to map domain compositions and phase boundaries in mixtures. Additional development of model independent methods to characterize domains (*e.g.* Pencer *et al.*, 2006*a*) is also underway.

APPENDIX *A*
Decoupled bilayers

When domains on the inner and outer bilayer leaflets are no longer in register, or become completely decoupled, the scattering amplitude can be calculated as

$$\begin{aligned}\int U(\mathbf{r})\exp(-i\mathbf{q}\cdot\mathbf{r})\,\mathrm{d}^3\mathbf{r} &= \frac{2}{q}Z_W(q,R)+\frac{1}{q}Z_{0,\mathrm{in}}(q,R)X_0(\alpha_{\mathrm{in}})\\ &+\frac{1}{q}\sum_{l=1}^{\infty}(2l+1)P_l\big(\cos\theta_{q,\mathrm{in}}\big)Z_{l,\mathrm{in}}(q,R)X_l(\alpha_{\mathrm{in}})\\ &+\frac{1}{q}Z_{0,\mathrm{out}}(q,R)X_0(\alpha_{\mathrm{out}})\\ &+\frac{1}{q}\sum_{l=1}^{\infty}(2l+1)P_l\big(\cos\theta_{q,\mathrm{out}}\big)Z_{l,\mathrm{out}}(q,R)X_l(\alpha_{\mathrm{out}}),\end{aligned}\quad(45)$$

where α_{in} and α_{out} are the angles defining the domains on the inner and outer leaflets (see Fig. 8), $\theta_{q,\mathrm{in}}$ and $\theta_{q,\mathrm{out}}$ are the angles between the scattering vector $\mathbf{q}$ and the axes of the domains. The functions $Z(q,R)$ and $X(\alpha)$ are as before, except that $Z_{\mathrm{in}}(q,R)$ and $Z_{\mathrm{out}}(q,R)$ are evaluated only on the inner and outer monolayers, respectively.

If we assume that the domains freely diffuse with respect to one another, then the orientation averaged scattered intensity is calculated as

$$\begin{aligned}\frac{1}{2}\int\left[\int U(\mathbf{r})\exp(-i\mathbf{q}\cdot\mathbf{r})\,\mathrm{d}^3\mathbf{r}\right]^2\sin\theta_q\,\mathrm{d}\theta_q &= \left\{\frac{2Z_W(q,R)+Z_{0,\mathrm{in}}(q,R)X_0(\alpha_{\mathrm{in}})+Z_{0,\mathrm{out}}(q,R)X_0(\alpha_{\mathrm{out}})}{q}\right\}^2\\ &+\frac{1}{q^2}\sum_{l=1}^{\infty}(2l+1)^2\big[Z_{l,\mathrm{in}}^2(q,R)X_l^2(\alpha_{\mathrm{in}})+Z_{l,\mathrm{out}}^2(q,R)X_l^2(\alpha_{\mathrm{out}})\big].\end{aligned}$$

Note that a number of possible cross terms vanish because of both the orthogonality of $P_l(x)$ and also because $\int P_l(x)\,\mathrm{d}x = 0$ for $l \neq 0$.

The same type of argument can be repeated for more than two rafts, considering of course that there is no interaction between the inner and outer rafts. For the order $l = 0$, we have

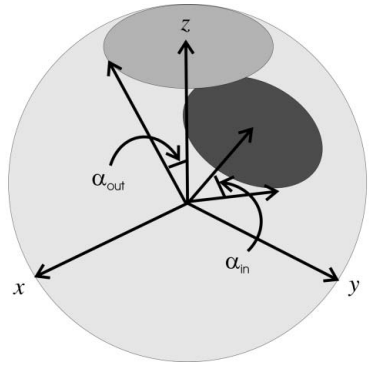

Figure 8
Schematic of a vesicle with inner and outer domains out of register. The inner domain is bounded by angle α_{in}, while the outer is bounded by α_{out}.

the square of the sum of contributions from all rafts, while for all orders $l \geq 1$, we have no mixed terms between apposing rafts, only square terms and correlation terms between inner (outer) rafts.

APPENDIX *B*
One annular domain

An important category of heterogeneous vesicle is that of the annular sector domain. In this case, instead of a circular raft, one has a 'circular band' (see Fig. 9). The problem is very similar to the circular raft case, the only difference being the evaluation of the angular component. Suppose that the annulus is bounded by angles α_1 and α_2, where α_1 is the angle corresponding to the smaller conical surface through the centre of the vesicle, and α_2, the angle corresponding to the larger one. In other words we have

$$w(\cos\theta) = 0 \quad \text{for} \quad 0 \leq \theta < \alpha_1, \tag{46}$$

$$w(\cos\theta) = 1 \quad \text{for} \quad \alpha_1 \leq \theta \leq \alpha_2 \tag{47}$$

and

$$w(\cos\theta) = 0 \quad \text{for} \quad \theta > \alpha_2. \tag{48}$$

In this case, one obtains

$$\begin{aligned} X_{l,\mathrm{ann}}(\alpha_1, \alpha_2) &= \int_{\alpha_1}^{\alpha_2} P_l(\cos\theta)\sin\theta\,\mathrm{d}\theta \\ &= \int_{0}^{\alpha_2} P_l(\cos\theta)\sin\theta\,\mathrm{d}\theta - \int_{0}^{\alpha_1} P_l(\cos\theta)\sin\theta\,\mathrm{d}\theta \\ &= X_l(\alpha_2) - X_l(\alpha_1). \end{aligned} \tag{49}$$

In contrast to the circular raft case, $\max_{l>l_0}(Y_l)$ decreases with l_0. There are no simple approximate formulae, except for the equatorial case, where

$$\begin{aligned} \alpha_1 &= \pi/2 - \beta, \\ \alpha_2 &= \pi/2 + \beta, \end{aligned} \tag{50}$$

with β small. In this case $X_{l,\mathrm{ann}}(\alpha_1, \alpha_2)$ is computed directly,

$$X_0(\alpha_1, \alpha_2) = 2\sin\beta. \tag{51}$$

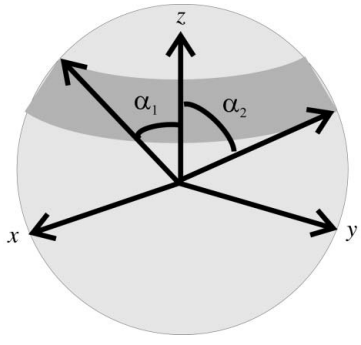

Figure 9
Schematic of a vesicle with an annular domain. The annulus is bounded by angles α_1 and α_2.

For $l \ll \pi/(2\beta)$, one can estimate the angular factor for small rafts,

$$\begin{aligned} X_{2l,\mathrm{ann}}(\alpha_1, \alpha_2) &\simeq 2(-1)^l \frac{1\times 3\times \ldots \times (2l-1)}{2\times 4\times \ldots \times 2l}\sin\beta, \\ X_{2l+1,\mathrm{ann}}(\alpha_1, \alpha_2) &\simeq 0. \end{aligned} \tag{52}$$

The rest of the calculation for a single annulus is completely analogous to the calculation for a single circular raft.

APPENDIX *C*
The SFF–Laplace method

ULVs are typically polydisperse in size (*e.g.* Pencer & Hallett, 2003; Kučerka *et al.*, 2004). Polydispersity is frequently taken into account in data fitting procedures, *via* convolution of the calculated intensity with a size distribution function. However, this process becomes fairly time-consuming, owing to the multiple integrations required in the calculation of the scattering curve. This problem can be avoided through the use of the separated form factors (SFF) approach (Kiselev *et al.*, 2002) together with a Laplace transform, presented recently by Pencer *et al.* (2006).

The integrated cross section given in §2.1 depends on the vesicle radius, R, through the form factors. For a polydisperse system it has the form

$$I(q) = \int G(R) I(q, R)\,\mathrm{d}R, \tag{53}$$

where $I(q, R)$ is defined in, for example, equation (50). The size distribution function, $G(R)$, can be represented by the Schulz distribution as follows,

$$G(R) = \left(\frac{z+1}{R_\mathrm{m}}\right)^{z+1} \frac{R^z}{\Gamma(z+1)} \exp\left[\frac{-R(z+1)}{R_\mathrm{m}}\right], \tag{54}$$

where R_m is a mean radius and the variance is $\sigma^2 = R_\mathrm{m}^2/(z+1)$.

Following the idea of the SFF method, when the thickness of the shell is much less than the vesicle radius, we can separate the parts corresponding to the symmetric bilayer and vesicle using a modified form of $Z_l(q, R_\mathrm{m})$ given by

$$Z_l(q, R_\mathrm{m}) = 2qR_\mathrm{m}^2 j_l(qR_\mathrm{m}) \int_0^{t/2} v(z)\cos(qz)\,\mathrm{d}z. \tag{55}$$

Employing the Laplace transform, as given by Pencer *et al.* (2006), we can write

$$I(q) = g_1\left(\sum_{l=0}^{\infty}(2l+1)^2[F_l^\mathrm{M}(q)]^2 \mathcal{L}\left\{u^{sR_\mathrm{m}-1}[F_l^\mathrm{TS}(q, R)]^2\right\}\right) \tag{56}$$

where $g_1 = s^{z+1}/\Gamma(z+1)$ and $s = (z+1)/R_\mathrm{m}$.

The form factor is then separated into the planar membrane form factor (that does not depend on a vesicle radius) and thin shell vesicle form factor. The planar membrane form factor is given by

$$F_0^{\rm M}(q) = \frac{8\pi}{q}\int_0^{t/2}[v(z)X_0(\alpha) + 2W(z)]\cos(qz)\,{\rm d}z,$$
$$F_l^{\rm M}(q) = \frac{8\pi}{q}\int_0^{t/2} v(z)\cos(qz)\,{\rm d}z, \qquad (57)$$

while the form factor corresponding to the thin shell with a radius $R_{\rm m}$ is given as

$$F_l^{\rm TS}(q, R_{\rm m}) = R_{\rm m}^2\, j_l(qR_{\rm m}). \qquad (58)$$

The Laplace transform can then be expressed as

$$\mathcal{L}\left\{u^{sR_{\rm m}-1}[F_l^{\rm TS}(q, R_{\rm m})]^2\right\} = \frac{\Gamma(4+2l+sR_{\rm m})}{\Gamma^2(3/2+l)}\frac{\pi q^{2l}}{4^{l+1}s^{4+2l+sR_{\rm m}}} \times {}_3F_2\left[1+l, \frac{4+2l+sR_{\rm m}}{2}, \frac{5+2l+sR_{\rm m}}{2}; \frac{3+2l}{2}, 2+2l; -\frac{4q^2}{s^2}\right], \qquad (59)$$

where ${}_3F_2$ is a generalized hypergeometric function (see, for example, Weisstein, 1998, 1999).

JP began this work while at the MPI for Colloids and Interfaces (MPIKG) and further developed it during his time at the NIST Center for Neutron Research (NCNR). He is grateful to Rumiana Dimova and Reinhard Lipowsky at the MPIKG and Susan Krueger at the NCNR for their support, encouragement and advice during these periods. The authors thank the reviewers, Thalia Mills, Richard Epand, Thad Harroun, Mu-Ping Nieh, John Nagle, and the members of the Cold Neutrons for Biology and Technology (CNBT) research partnership for valuable discussions during various stages of this project. We acknowledge the support of the National Institute of Standards and Technology, US Department of Commerce, in providing the neutron research facilities used in this work. The Advanced Foods and Materials Network (Networks of Centres of Excellence, Canada) is acknowledged for financial assistance.

References

Aragòn, S. R. & Pecora, R. (1976). *J. Chem. Phys.* **64**, 2395–2404.
Bagatolli, L. A. & Gratton, E. (2000). *Biophys. J.* **78**, 290–305.
Baumgart, T., Hess, S. T. & Webb, W. W. (2003). *Nature (London)*, **425**, 821–824.
Czeslik, C., Erbes, J. & Winter, R. (1997). *Europhys. Lett.* **37**, 577–582.
Dietrich, C., Bagatolli, L. A., Volovyk, Z. N., Thompson, N. L., Levi, M., Jacobson, K. & Gratton, E. (2001). *Biophys. J.* **80**, 1417–1428.
Dijck, P. W. M. van, Kaper, A. J., Oonk, H. A. J. & de Gier, J. (1977). *Biochim. Biophys. Acta*, **470**, 58–69.
Edidin, M. (2001). *Trends Cell Biol.* **11**, 492–496.
Feigenson, G. W. & Buboltz, J. T. (2001). *Biophys. J.* **80**, 2775–2788.
Glinka, C. J., Barker, J. G., Hammouda, B., Krueger, S., Moyer, J. J. & Orts, W. J. (1998). *J. Appl. Cryst.* **31**, 430–441.
Harrison, S. C. (1969). *J. Mol. Biol.* **42**, 457–483.
Hirai, M., Hirai, H., Koizumi, M., Kasahara, K., Yuyama, K. & Suzuki, N. (2006). *Physica B*, **385–386**, 868–870.
Jacobson, K., Mouritsen, O. G. & Anderson, R. G. W. (2007). *Nature Cell Biol.* **9**, 7–14.
James, F. (2007). http://wwwinfo.cern.ch/asdoc/WWW/minuit/minmain/minmain.html.
Katsaras, J., Epand, R. F. & Epand, R. M. (1997). *Phys. Rev. E*, **55**, 3751–3753.
Kerker, M. (1969). *The Scattering of Light and Other Electromagnetic Radiation*. New York: Academic Press.
Kiselev, M. A., Lesieur, P., Kisselev, A. M., Lombardo, D. & Aksenov, V. L. (2002). *Appl. Phys. A*, **74**(Suppl.), S1654–S1656.
Kline, S. R. (2006). *J. Appl. Cryst.* **39**, 895–900.
Knoll, W., Haas, J., Stuhrmann, H. B., Füldner, H.-H., Vogel, H. & Sackmann, E. (1981). *J. Appl. Cryst.* **14**, 191–202.
Korlach, J., Schwille, P., Webb, W. W. & Feigenson, G. W. (1999). *Proc. Natl Acad. Sci.* **96**, 8461–8466.
Kučerka, N., Liu, Y., Chu, N., Petrache, H. I., Tristram-Nagle, S. & Nagle, J. F. (2005). *Biophys. J.* **88**, 2626–2637.
Kučerka, N., Nagle, J. F., Feller, S. E. & Balgavý, P. (2004). *Phys. Rev. E*, **69**, 051903(1–7).
Lebedev, N. N. (1972). *Special Functions and Their Applications*. New York: Dover.
Li, L. & Cheng, J.-X. (2006). *Biochemistry*, **45**, 11819–11826.
McLachlan, N. W. (1955). *Bessel Functions for Engineers*. Oxford University Press.
Masui, T., Imai, M. & Urakami, N. (2006). *Physica B*, **385–386**, 821–823.
Mayor, S. & Rao, M. (2004). *Traffic*, **5**, 231–240.
Moody, M. F. (1975). *Acta Cryst.* A**31**, 8–15.
Nagle, J. F. & Tristram-Nagle, S. (2000). *Biochim. Biophys. Acta*, **1469**, 159–195.
Newton, R. G. (2002). *Scattering Theory of Waves and Particles*. New York: Dover.
Nicolini, C., Thiyagarajan, P. & Winter, R. (2004). *Phys. Chem. Chem. Phys.* **6**, 5531–5534.
Pencer, J., Anghel, V. N. P., Kučerka, N. & Katsaras, J. (2006*a*). *J. Appl. Cryst.* **39**, 791–796.
Pencer, J. & Hallett, F. R. (2003). *Langmuir*, **19**, 7488–7497.
Pencer, J., Krueger, S., Adams, C. & Katsaras, J. (2006). *J. Appl. Cryst.* **39**, 293–303.
Pencer, J., Mills, T., Anghel, V., Krueger, S., Epand, R. M. & Katsaras, J. (2005). *Eur. Phys. J. E*, **18**, 447–458.
Pencer, J., White, G. F. & Hallett, F. R. (2001). *Biophys. J.* **81**, 2716–2728.
Sears, V. F. (1989). *Neutron Optics – Introduction to the Theory of Neutron Optical Phenomena and their Applications*. Oxford University Press.
Sears, V. F. (1992). *Neutron News*, **3**, 726–737.
Veatch, S. L. & Keller, S. L. (2003). *Biophys. J.* **84**, 725–726.
Veatch, S. L., Leung, S. S. W., Hancock, R. E. W. & Thewalt, J. L. (2007). *J. Phys. Chem. B*, **111**, 502–504.
Veatch, S. L., Polozov, I. V. Gawrisch, K. & Keller, S. L. (2004). *Biophys. J.* **86**, 2910–2922.
Weisstein, E. W. (1998). *CRC Concise Encyclopedia of Mathematics*. New York: CRC Press.
Weisstein, E. W. (1999). *Generalized Hypergeometric Function*, from *MathWorld: A Wolfram Web Resource*, CRC Press LLC, and Wolfram Research, http://mathworld.wolfram.com/GeneralizedHypergeometricFunction.html.
Yanagisawa, M., Imai, M., Masui, T., Komura, S. & Ohta, T. (2007). *Biophys. J.* **92**, 115–125.